Inorganic Chemistry

pubs.acs.org/IC

Article

Insight into Potassium Vanadates as Visible-Light-Driven Photocatalysts: Synthesis of V(IV)-Rich Nano/Microstructures for the Photodegradation of Methylene Blue

Małgorzata Nadolska, Mariusz Szkoda, Konrad Trzciński, Paweł Niedziałkowski, Jacek Ryl, Aleksandra Mielewczyk-Gryń, Karolina Górnicka, and Marta Prześniak-Welenc*

Cite This: *Inorg. Chem.* 2022, 61, 9433−9444

Read Online

ACCESS | Metrics & More | Article Recommendations | Supporting Information

ABSTRACT: Photocatalysis is regarded as a promising tool for wastewater remediation. In recent years, many studies have focused on investigating novel photocatalysts driven by visible light. In this study, $K_2V_6O_{16}{\cdot}nH_2O$ nanobelts and KV_3O_8 microplatelets were synthesized and investigated as photocatalysts. Samples were obtained via the facile method based on liquid-phase exfoliation with ion exchange. By changing the synthesis temperature (20−80 °C), different compositions, morphologies, and V^{4+}/V^{5+} ratios were obtained and investigated as photocatalysts for organic dye degradation. Potassium vanadates' structural, morphological, and optical properties were characterized using X-ray diffraction(XRD), Fourier transform infrared spectroscopy (FTIR), X-ray photoelectron spectroscopy (XPS), Physical Property Measurement System (PPMS), thermogravimetric analysis (TGA) with mass spectrometry (MS), N_2 adsorption, scanning electron microscopy (SEM), photoluminescence (PL), and UV−vis diffuse reflectance spectroscopy (DRS). Synthesized $K_2V_6O_{16}{\cdot}nH_2O$ and KV_3O_8 showed an efficient absorption in the visible wavelength region with a narrow band gap energy of 1.80 and 1.91 eV, respectively. Their photocatalytic activity was evaluated by the degradation of methylene blue (MB) under simulated solar light illumination. The KV_3O_8 microplatelets exhibited the greatest photocatalytic activity, resulting in more than 90% degradation of the dye within the first 30 min. It is suggested that the observed excellent photocatalytic performance is attributed to the high content of V^{4+} species. Furthermore, the influence of active species was investigated, and the mechanism responsible for the photodegradation of the MB dye was discussed for the first time for potassium vanadates.

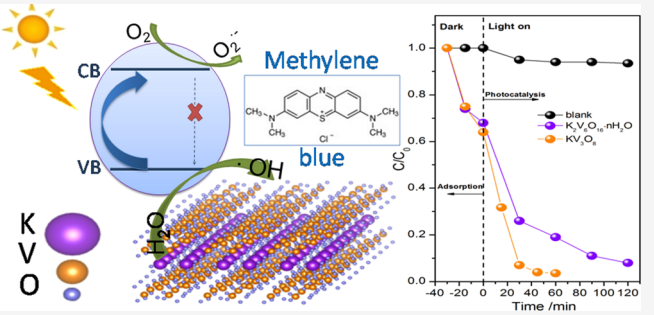

INTRODUCTION

The search for new, efficient, and low-cost photocatalysts has attracted increasing attention due to their perfect utilization of clean and renewable solar energy for treating wastewaters. In the past years, various materials have been investigated and tested for water purification.[1−4] Examples include metal[5,6] and metal oxide nanoparticles,[7] sulfides,[8,9] nitrides,[10] metal−organic frameworks,[11,12] or carbon-based nanostructures.[13] Recent studies demonstrate that metal vanadates exhibit promising visible-light photocatalytic reactivity in decomposing pollutants and water splitting.[14−17] A series of compounds can be mentioned here, such as Ag_3VO_4,[18] AgV_7O_{18},[19] CuV_2O_6,[20] $FeVO_4$,[21] $Cd_2V_2O_7$,[22] $InVO_4$,[23] $GdVO_4$,[24] and $BiVO_4$[25,26] as the most known representatives from the vanadate family. The conducted research is mainly devoted to the nanostructured vanadates, which can appear in various forms such as nanoparticles,[27,28] nanobelts,[29,30] or nanotubes.[31] It is well known that the shape and size play a significant role, as broadly described in the literature.[32−35] The photocatalytic properties are also strongly dependent on the crystalline structure. Generally, the monoclinic scheelite $BiVO_4$ (m-$BiVO_4$) is considered to be more active than the other two tetragonal phases.[36−38] In addition, the face-dependent photocatalytic behavior was also shown with the beneficial effect of (040) facets on contaminant degradation.[39−42] Another critical factor in the photocatalytic reaction is crystal defects, for example, oxygen vacancies, which trap photogenerated pairs and reduce their recombination rate.[43] The presence of oxygen vacancies can also broaden the activity range of a semiconductor oxide from UV to NIR light.[44] As a result, new pathways to synthesize photocatalysts with controllable properties are sought.

Received: January 14, 2022
Published: June 10, 2022

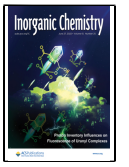

In this study, we present a new synthesis method of potassium vanadates as efficient photocatalysts for methylene blue (MB) degradation. Potassium vanadates were prepared by the facile LPE-IonEx method (liquid-phase exfoliation with ion exchange), which was recently proposed by our group.[63] LPE-IonEx is a straightforward, low-temperature, one-pot approach for the synthesis for transition metal oxide bronzes with controlled structural and morphological properties. Notably, the proposed method uses water as a solvent, making it eco-friendly. We demonstrated that, depending on the synthesis temperature (20−80 °C), the hydrated single-phase $K_2V_6O_{16}\cdot nH_2O$ to nonhydrated KV_3O_8 can be obtained through their mixture. In addition, an increase in temperature leads to increased V^{4+} concentration. The photocatalytic activity of prepared materials was evaluated by the degradation of an organic dye—methylene blue—in water under simulated solar light illumination. So far, KV_3O_8 has been considered as a precursor for V_3O_7 nanobelt synthesis for photocatalytic water splitting applications.[45] To the best of our knowledge, the photocatalytic properties of nonhydrated phase KV_3O_8 have never been investigated. Furthermore, the mechanism and kinetics of photocatalytic degradation were studied for the first time.

EXPERIMENTAL SECTION

Synthesis. Potassium formate (99%, Sigma Aldrich) and V_2O_5 (99.2%, Alfa Aesar) without further purification were used as reagents. Milli-Q deionized water was used (resistivity >19 MΩ·cm). The samples were prepared via the LPE-IonEx method, where the procedure was as follows: 500 mg of V_2O_5 was added to 50 mL of a 1 M solution of potassium formate in deionized water. The mixture was vigorously stirred for 72 h, and the synthesis was conducted in four temperatures: 20, 40, 60, and 80 °C. The samples were labeled according to the reaction temperature as KVO-20, KVO-40, KVO-60, and KVO-80, respectively. From the obtained solution, rusty red to burnt orange to orange precipitations were collected by centrifugation. After washing several times with deionized water, products were dried overnight at 40 °C under reduced pressure (0.01 bar).

Physicochemical Characterization. The X-ray diffractograms (XRD) were collected on a BrukerD2 Phaser diffractometer with Cu Kα radiation (λ = 1.5404 Å) in the range 2θ of 5−70° at room temperature. The samples' morphology was studied at room temperature by an FEI Quanta FEG 250 scanning electron microscope (SEM) in secondary electron mode using an Everhart-Thornley detector (ETD). Fourier transform infrared (FTIR) spectra were measured on a Perkin Elmer Frontier spectrophotometer. The KBr pellet method was used, and transmittance spectra were recorded from 4000 to 500 cm^{-1} with a resolution of 4 cm^{-1}. The high-resolution X-ray photoelectron spectroscopy (XPS) analysis was performed using an Escalab 250Xi device (ThermoFisher Scientific, USA) equipped with a monochromatic Al Kα source. Measurements were carried out at 25 eV pass energy with 0.05 eV energy step size. The X-ray spot size was 250 μm. The calibration of the XPS spectrum was done using the characteristic peak of adventitious carbon C 1s at 284.6 eV.[46] Thermogravimetric analysis (TGA) was carried out under an argon atmosphere with a flow rate 60 mL min^{-1} in the temperature range of 40−400 °C (with a heating rate of 5 °C min^{-1}) using Netzsch STA449 F1. A constant sample mass (20 ± 0.5 mg) was used. The thermal behavior has also been studied by EGA−MS (evolved gas analysis−MS). The gases that come out from the sample during heating were monitored by the quadruple mass spectrometer Netzsch QMS 403 Aëolos. The differential scanning calorimetry (DSC) measurement was performed under an argon atmosphere with a flow rate 60 mL min^{-1} in the temperature range of 35−450 °C (with a heating rate of 15 °C min^{-1}) using a NETZSCH DSC 204 F1 Phoenix calorimeter.

Nitrogen adsorption−desorption isotherms were measured on a surface area analyzer (NOVAtouch 2, Quantachrome Instruments) at 77 K. Before the measurements, samples were degassed under a dynamic vacuum at 40 °C for 12 h. The specific surface area was calculated using the Brunauer−Emmett−Teller (BET) linear equation in the relative pressure range (p/p_0) from 0.1 to 0.3. The correlation coefficient of the linear regression was not less than 0.99.

The UV−vis reflectance spectra of the selected materials were measured with a UV−vis spectrophotometer (Lambda 35, Perkin-Elmer) equipped with a diffuse reflectance accessory. The spectra were registered in a range of 300−900 nm with a scanning speed of 120 nm min^{-1}. Band gap energy values were determined as the intercept of the tangent of the plot of transformation of the Kubelka−Munk function. To determine the energy band gap (E_{bg}) of the chosen powders, the Kubelka−Munk function (eq 1) was applied:

$$f(\mathrm{KM}) = \frac{(1-R)^2}{2R} \tag{1}$$

where R is the reflectance.

The band gap was estimated by extrapolation of the linear region of $(f(\mathrm{KM})\ h\nu)^n$ vs $h\nu$ to $y = 0$, where the power "n" depends on the electron transition (n = 1/3, indirect forbidden (i.f.); n = 0.5, indirect allowed (i.a.); n = 2/3, direct forbidden (d.f.); and n = 2, direct allowed (d.a.)).[47] The photoluminescence spectra were recorded using 0.3 m Czerny−Turner spectrograph (SR303i, Andor) equipped with an ICCD camera (DH740, Andor). Powders were excited with UV LED (365 nm, 9 nm FWHM, 350 mW).

Magnetic Properties. Quantum Design Physical Property Measurement System (PPMS) with a vibrating sample magnetometer function was used to measure the temperature-dependent magnetic susceptibility (defined as $\chi = M/H$, where M is the magnetization and H is the applied field). The temperature dependence of the zero-field cooled (ZFC) magnetization was measured in the applied field of 3 T. Magnetic measurements were performed on a sample of arbitrary shape with a mass of about 10 mg.

Photocatalytic Activity. To evaluate the powders' photocatalytic activity, the degradation rate of methylene blue (MB) dye was monitored. Twenty milligrams of catalysts and 50 mL of an aqueous solution of MB ($C_0 = 10^{-5}$ M) were transferred to the beaker. Before irradiation, the suspension was magnetically stirred in the dark for 30 min to achieve adsorption/desorption equilibrium. Then, the suspension was irradiated with sunlight irradiation (a high-pressure 150 W xenon lamp, LOT−Quantum Design GmbH equipped with an AM1.5G filter) with constant magnetic stirring (150 rpm). The intensity of the light that reached the solution's surface was equal to 100 mW cm^{-2}. The changes of the concentration of MB (C) during decomposition were monitored using a UV−vis spectrophotometer at a wavelength of 665 nm. The quantitative evaluation of the role of the chemical individuals responsible for dye decomposition was performed using appropriate scavengers (1 mM of *tert*-butyl alcohol, benzoquinone, and ammonium oxalate).

The MB products after photocatalytic degradation using KVO-20 and KVO-80 samples were analyzed by ultra-performance liquid chromatography quadrupole time-of-flight mass spectrometry (UPLC−QTOF-MS/MS). The analysis of solutions obtained after photocatalytic degradation was performed on an Agilent 1290 Infinity liquid chromatograph and Agilent 6550 iFunnel Q-TOF LC/MS System. The mobile phase consisted of phase A: 0. 1% aqueous formic acid with 0.3% acetonitrile and phase B: 0.1% formic acid in acetonitrile. The analysis was recorded with a gradient elution from 0 to 100% B during 10 min with an injection volume of 5 μL. The Agilent ZORBAX RRHD Eclipse Plus C18 column (95 Å, 2.1 × 50 mm, 1.8 μm) was used for the separation and detection of resulting products with a column temperature of 24 °C and flow rate 0.3 mL/min. The mass spectra were obtained in positive modes using the following operating parameters: capillary voltage 3.5 kV, nozzle voltage 2 kV, and fragmentor voltage 175 V. The gas temperature was 250 °C with a flow rate of 12 L/min and nebulizer pressure of 40 psi; the sheath gas temperature was 300 °C with a flow rate 11 L/min.

https://doi.org/10.1021/acs.inorgchem.2c00136
Inorg. Chem. 2022, 61, 9433−9444

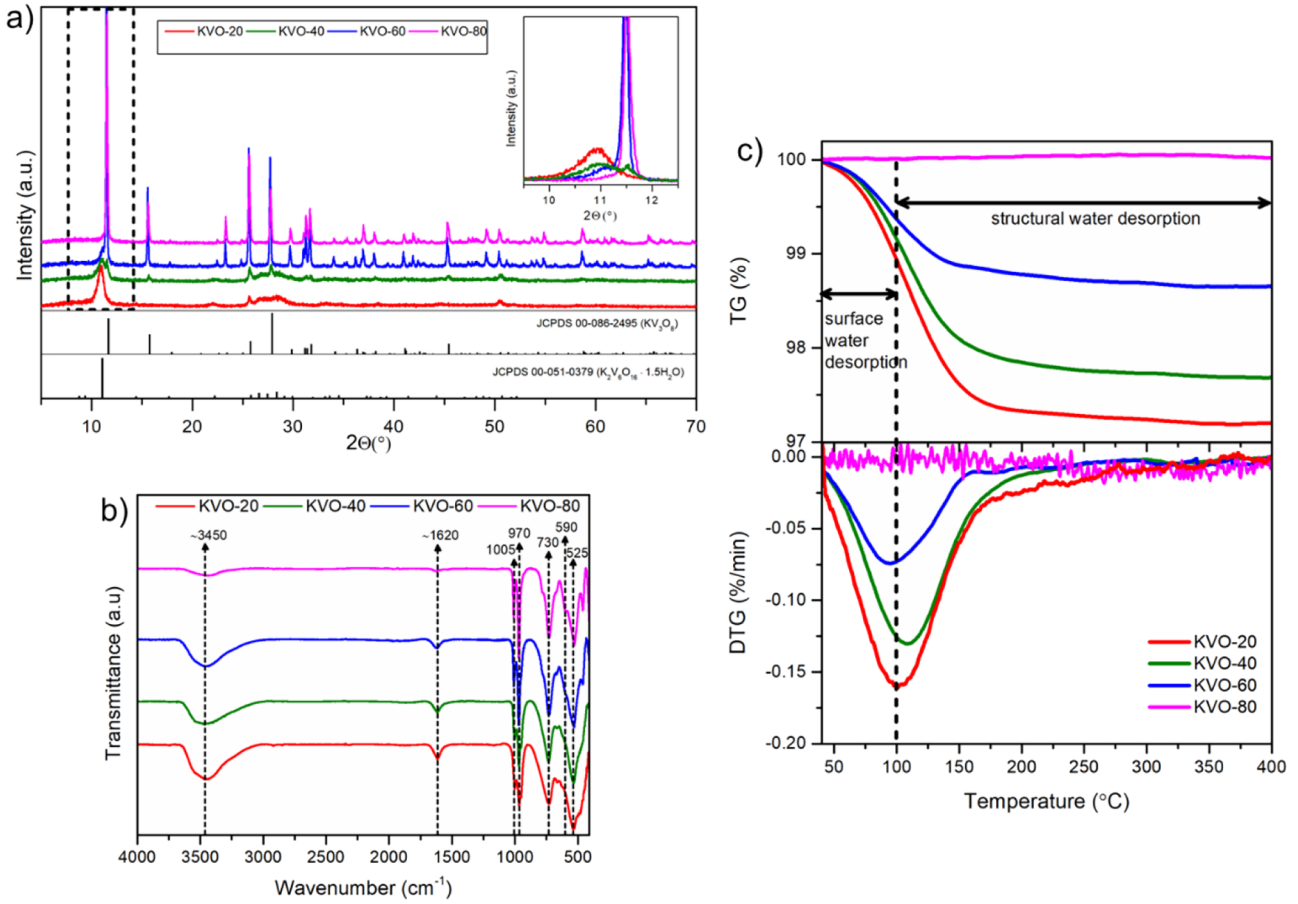

Figure 1. (a) XRD patterns, (b) FTIR spectra, and (c) TG and DTG curves of the samples obtained under different reaction temperatures. The inset shows the zoomed view of the XRD's most intense peaks ascribed to KV_3O_8 (JCPDS card no. 00-086-24-95) and $K_2V_6O_{16}\cdot 1.5H_2O$ (JCPDS card no. 00-051-0379).

The mass spectra were monitored in the range from 50 to 1000 m/z with a scan range of one spectrum per second. The obtained UPLC−QTOF-MS/MS data were analyzed using the Mass Hunter Qualitative Analysis software.

Electrochemical Characterization. The electrochemical measurements were performed using an Ivium Vertex potentiostat/galvanostat in a three-electrode cell using Pt mesh as the counter electrode and Ag/AgCl (3 M KCl) as the reference electrode. The tested powder was deposited onto degreased FTO (fluorine-doped tin oxide) using a dip-coating method according to the procedure described previously.[48] Measurements were performed in deaerated aqueous 0.2 M K_2SO_4. The Mott−Schottky analysis was performed to determine the flat band potential. The impedance spectra were recorded at a potential range from 0.4 to 0.9 V vs Ag/AgCl (3 M KCl). The potential was held before each spectrum registration to achieve a steady-state condition. The potential range for analysis was determined on the basis of a cyclic voltammetry (CV) curve. The space charge capacitance was determined from 1000 Hz frequency according to the formula $C_{sc} = 1/\omega Z''$.

RESULTS AND DISCUSSION

Structural Analysis. The X-ray diffractograms were recorded to confirm the phase purity and crystallinity of obtained samples (see Figure1a). For the diffractogram for the sample synthesized at 20 °C (KVO-20), all indices can be indexed within hydrated potassium vanadate phase $K_2V_6O_{16}\cdot 1.5H_2O$, JCPDS card no. 00-051-0379, which corresponds to a monoclinic structure with lattice parameter values of a = 12.29 Å, b = 3.59 Å, and c = 16.01 Å. The main diffraction peak, located at approximately 11°, corresponds to the diffraction from the (002) crystallographic plane of this phase. Moreover, no signals of other phases were detected, indicating the high purity of the sample. For the samples synthesized at higher temperatures, additional peaks can be observed, indicating the presence of the secondary phase KV_3O_8, JCPDS card no. 00-086-24-95, which corresponds to a monoclinic structure with lattice parameter values of a = 4.97 Å, b = 8.38 Å, and c = 7.64 Å. The presence of KV_3O_8 is revealed by its characteristic diffraction peak located at approximately 11.5°, which corresponds to the (001) crystallographic plane (see inset in Figure 1a). With increasing synthesis temperature, the intensity of the diffraction peaks ascribed to the KV_3O_8 phase increases, and the first peak of KVO-40 and KVO-60 is split. This suggests the existence of two phases in these samples. The XRD pattern of sample KVO-80 shows indexed reflection only for the KV_3O_8 phase. The characteristic peak for the hydrated potassium vanadate phase is no more visible. FTIR spectra of the samples are shown in Figure 1b and summarized in Table S1. The bands at ∼1005 and ∼970 cm^{-1} can be assigned to V═O vibrations, while those at 525 and 590 cm^{-1} can be assigned to the symmetric and asymmetric stretching of V−O−V.[49] The band at 730 cm^{-1} corresponds to bridging V−O···K stretching.[50] In all spectra, the splitting of the V═O bands can be observed. Such phenomenon implies the distortions in the vanadium oxide layers and the existence of VO_5 and VO_6 polyhedra, which are typical for hexavanadates and mixed-valence vanadium compounds.[51,52] Significant changes were

https://doi.org/10.1021/acs.inorgchem.2c00136
Inorg. Chem. 2022, 61, 9433−9444

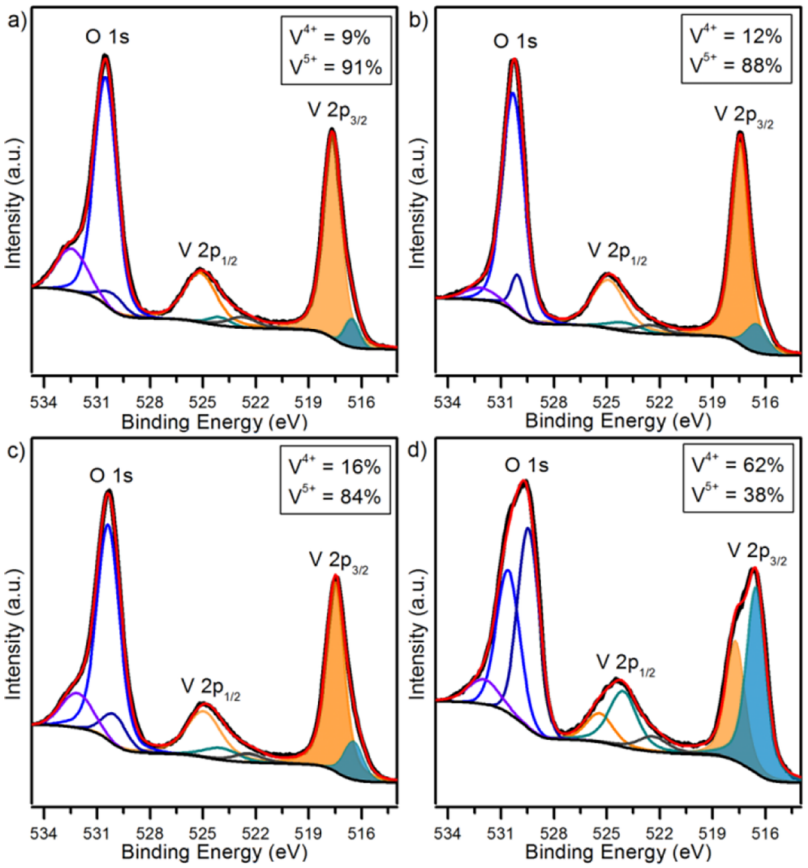

Figure 2. The XPS spectra of the O 1s and V 2p region of (a) KVO-20, (b) KVO-40, (c) KVO-60, and (d) KVO-80, respectively.

also observed in the position of the absorption band located ca. 1005 cm^{-1}. In comparison to KVO-20, the maximum for KVO-80 is shifted from 1000 to 1010 cm^{-1}. This is linked to the shortening of the bond length and reducing the distance between vanadium oxide layers. The distance between layers for the hydrated potassium vanadate ($K_2V_6O_{16}{\cdot}1.5H_2O$) is almost doubled than for the nonhydrated phase (KV_3O_8).[49,53,54] Also, in all spectra, there are two extra bands at ∼3450 and ∼1620 cm^{-1} that can be associated with water molecules' stretching and bending vibrations.[45] Their positions vary within the samples, and peaks shift to the low wavenumber from 1633 and 3475 cm^{-1} for KVO-80 to 1615 and 3435 cm^{-1} for KVO-20. According to the literature, a decrease in wavenumber is evidence of the binding of water with other atoms.[55] In case of anhydrous KV_3O_8 (KVO-80), physisorbed water molecules are only weakly bonded to the samples' surface, while for hydrated $K_2V_6O_{16}{\cdot}nH_2O$ (KVO-20), water molecules are trapped in the crystalline lattice by either interactions with potassium ion or vanadium-oxide layers. Moreover, in the KVO-20, KVO-40, and KVO-60 spectra, an additional band at 950 cm^{-1} can be observed. The position of this band suggests the existence of the OH bridge between two metals, probably between V.[56] Thermogravimetric measurements were performed to further investigate the weight percentage of crystalline water in samples (Figure 1c). According to the TG and DTG curves, the decomposition of the material occurred stepwise. Especially for single-phase, KVO-20 is seen on the DTG curve that a broad peak between 40 and 180 is asymmetric (which indicates two different decomposition kinetics) and overlaps with another broad one. Simultaneously, the molecular weight channels 17 (corresponding to OH) and 18 (H_2O) on the EGA−MS curves showed a broad peak ion current corresponding to the shape of the peak on the DTG curve (Supporting Information Figure S1a). The ratio of the integrated ionic current of m/z = 17 and 18 is around 0.2 in the whole temperature range, which corresponds to a well-known signature of water molecules.[57] Thus, the weight loss between 40 and 100 °C is attributed to the evaporation of physisorbed water and that between 100 and 400 °C to crystalline water.[58] The weight loss of crystalline water for a single-phase hydrated sample (KVO-20) is 1.75 wt %, which corresponds to 0.65 molecule of water per $K_2V_6O_{16}$ formula unit. The weight loss for KVO-40 and KVO-60 samples is smaller and equal to 1.48 and 0.72%, respectively. According to the XRD and FTIR results, these samples are composed of two phases: the hydrated and nonhydrated one. Therefore, upon comparison, the weight loss of the crystalline water in these samples will be smaller. The KVO-80 sample is thermally stable up to 350 °C, which is confirmed by DSC results where no thermal effects are visible (Supporting Information Figure S1b). The structural and thermal measurements confirmed that this sample consists of only a nonhydrated KV_3O_8 phase.

X-ray photoelectron spectroscopy (XPS) was used to assess the chemical composition and the charge state of vanadium ions in the studied samples. The high-resolution XPS spectra recorded in O 1s and V 2p binding energy regions (Figure 2a−d) show a complex shape of not less than three peaks located around 530 eV attributed to O 1s, as well as 517 and 524 eV attributed to the V $2p_{3/2}$ and V $2p_{1/2}$ peak doublet.[59] The V 2p peaks for all samples show an asymmetric shape with a very weak shoulder line shifted toward negative binding energies

https://doi.org/10.1021/acs.inorgchem.2c00136
Inorg. Chem. 2022, 61, 9433−9444

versus the primary component. Based on these findings, two different V components should be used for spectral deconvolution. The V $2p_{3/2}$ peaks at 516.5 and 517.5 eV correspond to V^{4+} and V^{5+}, respectively.[59] Finally, the O 1s satellite at 522 eV was also considered in the deconvolution model based on previous findings.[60] The XPS analysis allows one to estimate the relative share of vanadium V^{4+} to be on a similar level (9−16%) for the samples KVO-20, KVO-40, and KVO-60, whereas for the sample KVO-80, the vanadium V^{4+} valence state is dominant and equals 62%. The revealed significant difference in V^{4+} affects photocatalytic properties, originating from a narrow band gap of V^{4+} species facilitating charge carrier separation. The O 1s core-level spectra could be fitted by three components. The two most notable peaks at 530.1 and 530.5 eV are attributed to the O 1s orbitals of the O−V^{4+} and O−V^{5+} bonds, respectively, whose ratios are in good agreement with the V^{5+}/V^{4+} ratios estimated from the deconvolution of V $2p_{3/2}$. The third peak centered at 532.5 eV, observable for all samples, is ascribed to adsorbed OH^- ions on the surface.[61]

The above XPS analysis confirms the mixed-valence character of the obtained samples and the existence of V(IV) and V(V) in their structure. However, it should be borne in mind that XPS is a surface-sensitive technique and that the obtained results indicate a high content of V^{4+} on the surface (which is important in the view of catalytic action) and not in the bulk. Thus, to further investigate the valence of vanadium in the materials, static magnetic susceptibility was measured for samples obtained at the lowest (KVO-20) and highest temperature (KVO-80).

The temperature dependence of the magnetic susceptibility for KVO-20 and KVO-80 measured in an applied field of 3 T is shown in Figure 3. It can be clearly seen that for both samples

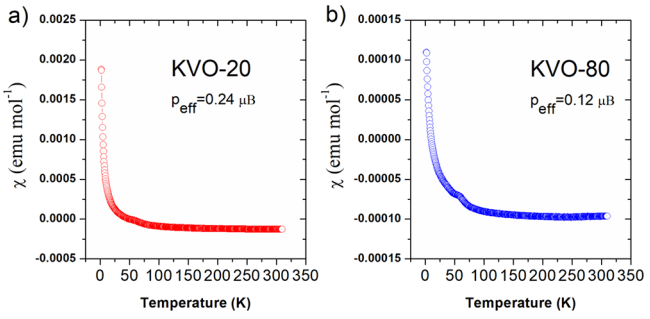

Figure 3. The temperature dependence of the magnetic susceptibility for (a) KVO-20 and (b) KVO-80 samples.

above about 50 K, $\chi(T)$ is weakly temperature-dependent and its magnitude is small. At low temperatures, the pronounced tail is observed, which can be attributed to the presence of a small amount of uncompensated V^{4+} ions.[62] To determine the effective magnetic moment (p_{eff}), the experimental data were fitted by the modified Curie−Weiss law, $\chi = \chi_0 + C/(T - \theta_P)$, where χ_0, C, and θ_P are the temperature-independent susceptibility, the Curie constant, and the paramagnetic Curie temperature, respectively. The fit gave C = 0.00712(3) emuK for KVO-20 and C = 0.00178(2) emuK for KVO-80. Assuming that the magnetic moment originates from V^{4+} only, the effective magnetic moment per V can be obtained using the relation $p_{eff} = (3Ck_B/\mu_B^2 N_A)^{1/2}$, where k_B is the Boltzmann constant, μ_B is the Bohr magneton, and N_A is Avogadro's number. The resulting effective magnetic moment p_{eff} is 0.24 and 0.12 μ_B/V for KVO-20 and KVO-80, respectively. The calculated effective magnetic moments are much smaller than the expected value of p_{eff} = 1.73 μ_B for the free V^{4+} ion. Thus, obtained results suggest that the samples consist of a vast majority of nonmagnetic V(V) species and only a small fraction of V(IV) located on the sample surface or between crystalline grains, and in case of bulk samples, the V^{4+}/V^{5+} ratio is smaller than that on the surface.

The morphologies of the samples undergo significant temperature evolution. The sample KVO-20 (single-phase $K_2V_6O_{16}\cdot 0.65H_2O$ according to XRD, FTIR, and TG results) consists of belt-like structures with a width between 50 and 200 nm, a thickness of 10−40 nm, and a length of a few micrometers (Figure 4a,b). With the increase of the synthesis temperature, the $K_2V_6O_{16}\cdot 0.65H_2O$ nanobelts become thinner, and their cross-sections decrease. For samples KVO-40 and KVO-60, the width of $K_2V_6O_{16}\cdot 0.65H_2O$ nanostructures is between 30 and 50, 20 and 40, and 10 and 20 nm, respectively, while the thickness of nanobelts is below 10 nm. Moreover, the $K_2V_6O_{16}\cdot 0.65H_2O$ nanobelts' length decreases from a few micrometers (sample KVO-40) to 100−250 nm (sample KVO-60). The crystals of the secondary phase (KV_3O_8) exhibit a plate-like morphology, and for sample KVO-40 (Figure 4c,d), the width of plates is between 0.5 and 2.5 μm, the length is between 0.5 and 4 μm, and the thickness is about 50 nm. With increasing synthesis temperature (sample KVO-60 and KVO-80), the length of KV_3O_8 crystal rises up to 0.5−7 and 1−10 μm, respectively, and the width of crystals equals ca. 150 nm. The thickness of KV_3O_8 crystals in the single-phase sample KVO-80 (Figure 4g,h) is more uniform and equals 150 nm, whereas for the multiphase sample KVO-60 (Figure 4e,f), it is in the range between 50 and 350 nm. Moreover, the

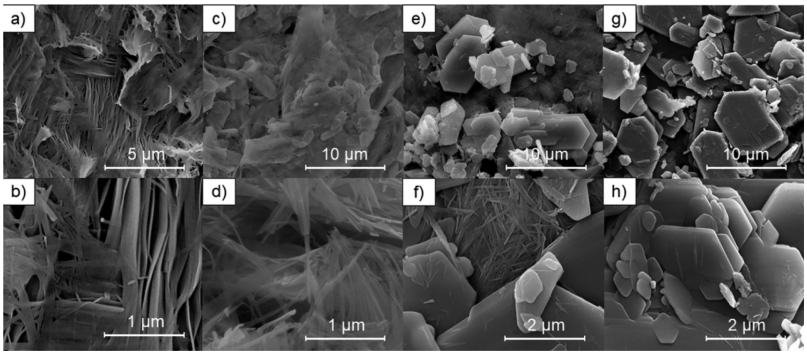

Figure 4. SEM images of samples (a, b) KVO-20, (c, d) KVO-40, (e, f) KVO-60, and (g, h) KVO-80.

https://doi.org/10.1021/acs.inorgchem.2c00136
Inorg. Chem. 2022, 61, 9433−9444

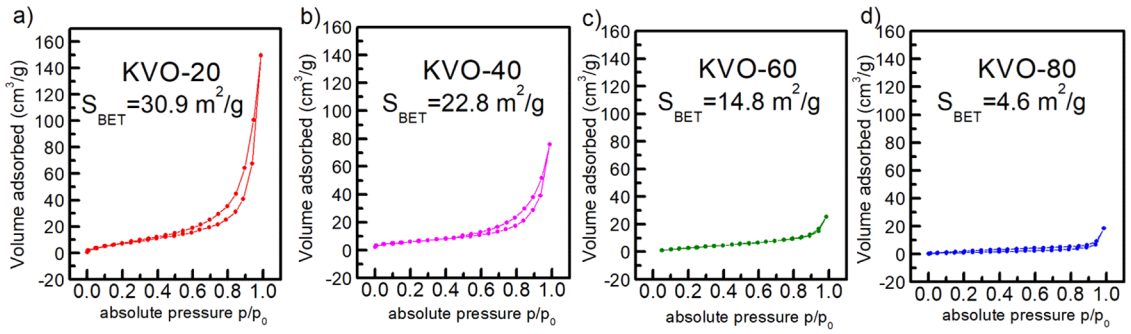

Figure 5. N_2 adsorption−desorption isotherm and calculated surface area for (a) KVO-20, (b) KVO-40, (c) KVO-60, and (d) KVO-80.

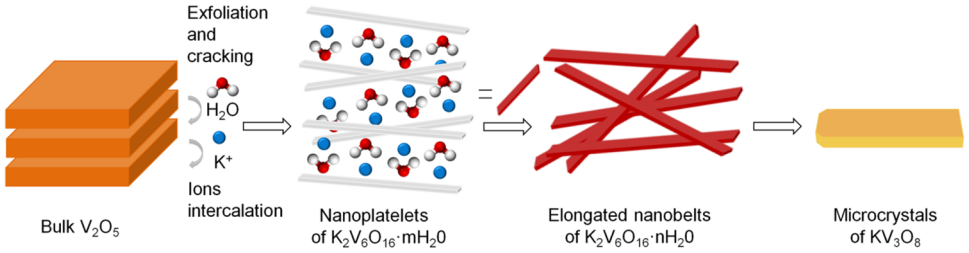

Figure 6. Schematic illustration of the evolution of potassium vanadate morphology.

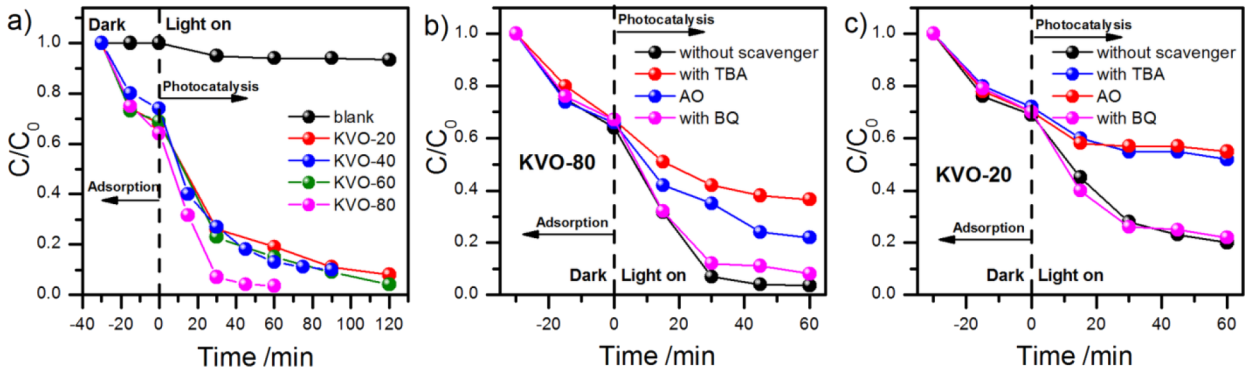

Figure 7. (a) The C/C_0 vs t plot representing the photocatalytic degradation of MB for all tested samples. (b, c) The effect of scavengers on the MB degradation rate for single-phase samples KVO-80 (KV_3O_8) and KVO-20 ($K_2V_6O_{16}{\cdot}0.65H_2O$), respectively.

surface areas of samples were determined through N_2 adsorption and BET analysis (Figure 5). As expected, the highest surface area (30.9 m^2/g) has been noted for KVO-20 with a nanostructural morphology and the lowest (4.6 m^2/g) for KVO-80 with microplatelets.

The schematic illustration of the evolution of potassium vanadate morphology is presented in Figure 6. The synthesis reaction is based on the intercalation of the solvent molecule into layer spacing and its further exchange with alkali metal ions. The reaction scheme of KVO by the LPE-IonEx synthesis method is similar to the ammonium metavanadate synthesis reported previously.[63] The solid vanadium oxide underwent delamination by the insertion of water molecules into the interlayer space. The H_2O molecules are partially trapped during potassium ion intercalation, and hydrated potassium vanadate ($K_2V_6O_{16}{\cdot}mH_2O$) is formed. During the synthesis at room temperature, the water stoichiometry is stabilized and elongated nanobelts ($K_2V_6O_{16}{\cdot}nH_2O$) are obtained. The KV_3O_8 microcrystals are formed via the dehydration and recrystallization of $K_2V_6O_{16}{\cdot}mH_2O$ at higher synthesis temperatures because the exchange between solvent molecule and potassium ion is more efficient, and a nonhydrated phase is obtained: KV_3O_8. Throughout the dehydration process, the c axis of the crystal unit cell is decreased by almost half. During this process, the creation of V^{4+} species is probable. Therefore, the obtained KV_3O_8 phase possesses a rich vanadium-defective structure.

Photocatalytic Properties. The photocatalytic performance of investigated powders is presented as a C to C_0 ratio in Figure 7a. Additionally, the effect of the photolysis of MB is added for comparison (blank). Before the irradiation, methylene blue was adsorbed on the surface of the tested powders at a similar, considerable level of 30%. Adsorption is an essential process in photocatalysis, which enriches the pollutants around the catalyst surface, and often, strong adsorption results in increased photocatalytic performance.[64] All samples acted as efficient photocatalysts for dye decomposition; however, the sample obtained at 80 °C exhibited the highest photoactivity. After about 30 min of exposure, over 90% of MB was degraded. In the case of the rest of the samples (obtained at 20, 40, and 60 °C), the observed photoactivity was similar and the time required for MB degradation was longer (approximately 90% of degradation after 90 min). To the best of our knowledge, there is only one

https://doi.org/10.1021/acs.inorgchem.2c00136
Inorg. Chem. 2022, 61, 9433−9444

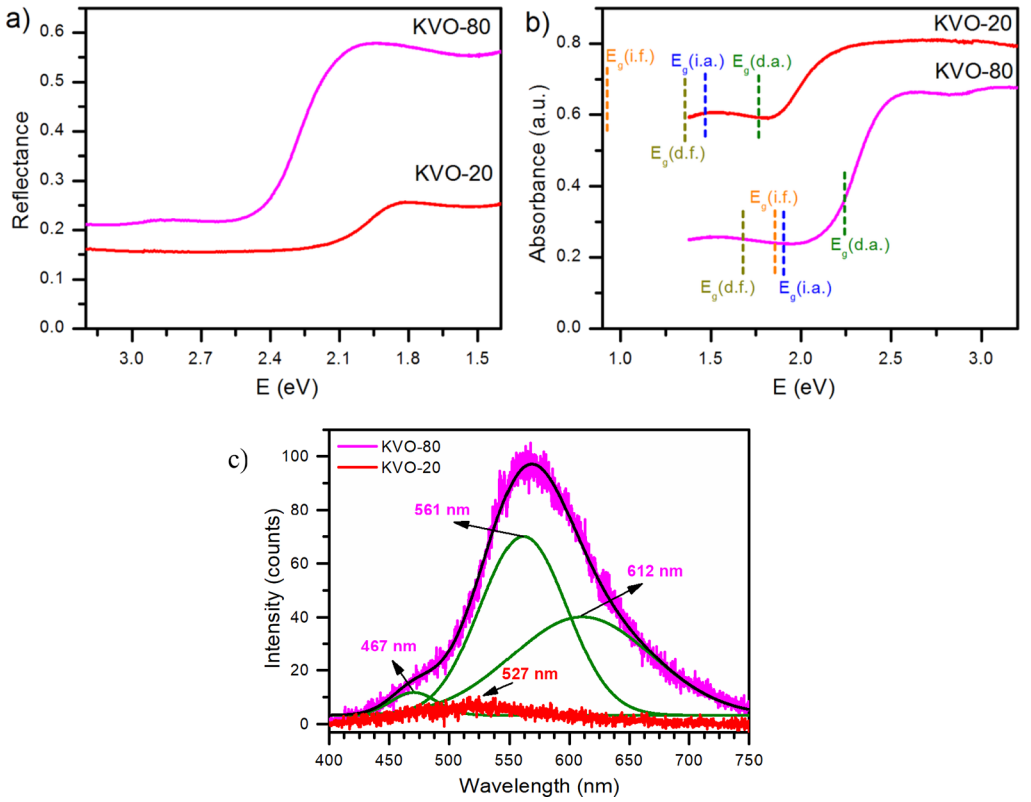

Figure 8. (a) Reflectance (measured) and (b) absorbance (calculated) spectra of KV_3O_8 microplatelet (KVO-80) and $K_2V_6O_{16}{\cdot}0.65H_2O$ nanobelt (KVO-20) samples. (c) Photoluminescence spectra of KV_3O_8 (KVO-80) and $K_2V_6O_{16}{\cdot}0.65H_2O$ (KVO-20).

report[65] devoted to the potassium vanadate compounds that presents using of hydrated vanadates ($K_2V_6O_{16}{\cdot}1.5H_2O$/$2.7H_2O$) for the photodegradation of methyl orange. In comparison to the mentioned work, samples obtained by our method exhibit better photocatalytic activity. Furthermore, the calculated band gap for $K_2V_6O_{16}{\cdot}nH_2O$ is narrower in the case of the sample reported by us. Moreover, herein, for the first time, we present nonhydrated KV_3O_8 as a new efficient photocatalyst. This implies that the photocatalytic efficiency of our samples results from the specific structural properties, which were provided by the proposed innovative LPE-IonEx method. Often, the developed surface also has a beneficial effect for photocatalytic efficiency. It is reported that a high surface area inhibits the electron−hole recombination and allows the adsorption of more MB molecules.[66−68] Nonetheless, for investigated samples, the reverse tendency was observed. The sample with the lowest surface area (according to the BET method) exhibited the best photocatalytic performance, while for the sample with the highest surface area, the degradation process was the least effective. This confirms that, in the case of the synthesized samples, their photocatalytic activity is not dependent on the surface area. It is supposed that the presence of V^{4+} species plays a pivotal role here. Surface defect engineering has gained a lot of attention in the development of efficient photocatalysts. The existence of defect sites in vanadates has been reported to be crucial in enhancing photocatalytic performance in water splitting and degradation of pollutants.[69−71] Zhang et al. have shown enhanced photoelectrochemical performance of V^{4+} self-doped m-$BiVO_4$. Compared to the pure $BiVO_4$, V^{4+} doped samples possess enhanced photocurrent density, smaller charge transfer resistance, longer electron lifetime, and improved separation of photogenerated electrons and holes.[72] Yu and co-workers presented CaV_2O_6 nanorods that exhibited improved photocatalytic activity in MB degradation due to the coexistence of V^{4+}/V^{5+} in the lattice. CaV_2O_6 shows an indirect allowed electronic transition with a band gap energy of 2.56 eV and hydroxyl radicals as the major active species.[73] Saputera et al. obtained $BiVO_4$ with a different vanadium vacancy content by changing the calcination temperature after sol−gel synthesis. Obtained samples were then evaluated by the degradation of palm oil mill effluent waste under UV−visible light. Results revealed that the higher the V^{4+} content was, the better were the degradation rates and reaction rate constant. It was also observed that the increase in V^{4+} content resulted in a slight increase of band gap energy (2.44 to 2.50 eV).[74]

To investigate the kinetics of the process, the $\ln(C/C_0)$ vs t plot was prepared (see Supporting Information Figure S2). The most probable is the pseudo-first-order kinetics according to the Langmuir−Hinshelwood model;[75] however, the mechanism of the photocatalytic degradation can be more complex. Thus, the additional measurements for single-phase samples $K_2V_6O_{16}{\cdot}0.65H_2O$ (KVO-20) and KV_3O_8 (KVO-80) in the presence of appropriate scavengers were performed (see Figure 7b,c). *tert*-Butyl alcohol (TBA), benzoquinone (BQ), and ammonium oxalate (AO) act as a hydroxyl radical, superoxide radical, and hole scavenger, respectively.[76] The decrease of the decomposition efficiency in a solution containing a scavenger suggests the role of the relevant species in the mechanism of the degradation mechanism. Thus, in both cases, the role of superoxide radicals is negligible. On the other hand, degradation efficiency in the presence of a hydroxyl radical scavenger is significantly diminished in comparison with the control measurement. It is indirect

https://doi.org/10.1021/acs.inorgchem.2c00136
Inorg. Chem. 2022, 61, 9433−9444

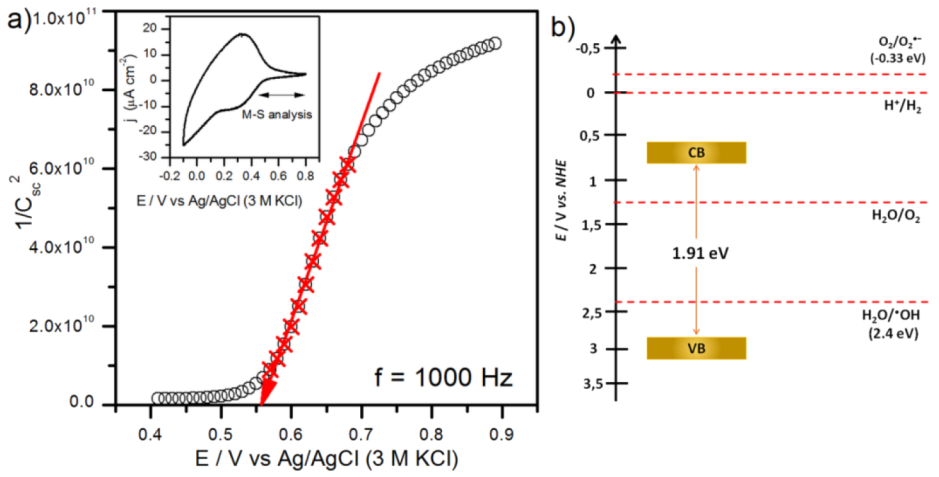

Figure 9. (a) The Mott−Schottky analysis performed for KV_3O_8 (KVO-80). Inset: cyclic voltammetry curve recorded with 50 mV/s. (b) The energy band position diagram of the sample KV_3O_8 (KVO-80).

proof that OH· is formed during the illumination of the $K_2V_6O_{16}·0.65H_2O$ (KVO-20) and KV_3O_8 (KVO-80) aqueous suspensions. Noteworthily, the direct oxidation of MB by photoexcited holes from the valence band of the photocatalyst also takes part in the degradation process. According to the results presented in Figure 7b, it can be concluded that approximately equal amounts of MB are decomposed by OH radicals and holes in the case of $K_2V_6O_{16}·0.65H_2O$. The role of direct oxidation in the case of KV_3O_8 is smaller but still significant (Figure 7c).

Optical Properties of $K_2V_6O_{16}·0.65H_2O$ Nanobelts and KV_3O_8 Microplatelets. The optical behavior of single-phase samples KV_3O_8 microplatelets and $K_2V_6O_{16}·0.65H_2O$ nanobelts, which were, respectively, the most and the least photoactive material, was further examined using UV−vis spectroscopy in the reflectance mode. The spectra of both samples are presented in Figure 8a. As can be seen, synthesized materials absorb a significant part of the light in the visible range. This feature is beneficial for the materials used in photocatalysis. Reflectance edges seen on both spectra are related to the energy band gap transition, so the obtained results allowed the energy band gap to be estimated. There is no information about the type of electron transition; thus, all possibilities were taken into account, as presented in Figure S3. The absorbance spectra of both powders with marked band gaps estimated from $(f(\mathrm{KM})·h\nu)^n$ vs $h\nu$ plots are presented in Figure 8b. Since the energy band gap corresponds to the absorbed photons with the lowest energy, the direct energy band gap (d.a.) in the case of $K_2V_6O_{16}·0.65H_2O$ nanobelts is the most probable. On the other hand, the estimated value of the direct band gap for KV_3O_8 microplatelets corresponds to a wavelength that is already within the absorption edge. Thus, it is very likely that the optical band gap of the KV_3O_8 material is related to the allowed indirect transition (i.d.); nevertheless, the direct band gap can be taken into account as well. Thus, the determined direct energy band gaps for $K_2V_6O_{16}·0.65H_2O$ and KV_3O_8 are 1.80 and 2.23 eV (and the indirect energy band gap for KV_3O_8 is equal to 1.91 eV), respectively. These values are in accordance with the observed colors: dark red for the hydrated phase and orange for the nonhydrated phase. The differences in estimated energy band gaps suggest that KVO-20 could be a better photocatalyst due to the wider range of electromagnetic radiation that can be absorbed and converted. As shown in Figure 7, it is not the case. In the case of KV_3O_8 and $K_2V_6O_{16}·0.65H_2O$, direct comparison is misleading because they are two different compounds with different crystal structure and stoichiometry (Figure 1), surface composition (Figure 2), morphology (Figure 4), and surface area (Figure 5). It can be concluded that all the above-mentioned parameters have a greater impact on photoactivity than UV−vis absorption ability.

Additionally, the photoluminescence spectra have been recorded using UV excitation. Results are presented in Figure 8c. Generally, the emission spectrum of KVO-80 is characterized by a much higher intensity of photoluminescence in comparison with KVO-20. It could be simply related to the better crystallinity of the sample prepared at a higher temperature;[77] however, the shape of the emission bands is also different. Often, photocatalysts are examined with PL to compare emission intensity. In the case of photoactive materials, a higher PL intensity means a higher rate of recombination processes and therefore poorer photocatalytic performance. Thus, here PL spectra suggest that better photocatalytic activity should be observed for the KVO-20 sample (which is not true). However, such direct comparison can be done for samples with similar characteristics (composition, morphology, surface area, etc.) because PL intensity is affected by many parameters.[78]

The PL intensity of the KVO-20 spectrum is very low, which makes the analysis very difficult to perform. The maximum can be found at about 527 nm (2.35 eV). Taking into account the absorbance spectrum, the recorded emission is not related with conduction to valence band extinction. In the case of the KVO-80 sample, the spectrum can be deconvoluted to 3 Gaussian peaks with the maximum at 467 nm (2.66 eV), 561 nm (2.21 eV), and 612 nm (2.03 eV). The PL emission at energies lower than the band gap (2.03 eV) is related to the presence of states within the energy band gap. Here, it can be associated with the presence of oxygen vacancies and V(IV) centers seen on XPS. A similar phenomenon was observed for partially reduced metal oxides (TiO_2, SnO_2, and In_2O_3), while for fully oxidized materials, visible light photoluminescence was diminished.[79] The PL bands at energies lower than the energy band gap were also reported for V_2O_5 and were described as an effect of the oxygen vacancies' presence.[80] The second band at the PL spectrum of KVO-80 has an energy (2.21 eV, 561 nm) close to

https://doi.org/10.1021/acs.inorgchem.2c00136
Inorg. Chem. 2022, 61, 9433−9444

the band gap; thus, it probably originates from the direct band edge transition. The low-intensity band at 467 nm that can be seen in Figure 8c and a similar one were already reported for V_2O_5 nanostructures. It was described as the recombination of UV excited electrons from a higher level in the V 3d orbital (in the conduction band) to the ground level.[81]

Energy Band Position of KV_3O_8 (KVO-80). Electrochemical characterization of the sample allowed the estimation of the energy band position for the stable nonhydrated KV_3O_8 phase. The procedure of sample thin film preparation did not affect its crystal structure and the charge state of vanadium (see Supporting Information Figures S4 and S5). The flat band potential (E_{fb}) was determined using the Mott−Schottky (MS) analysis. To estimate the space charge region capacitance (C_{sc}), the impedance spectra were measured at dark conditions as a function of applied potential. The range of potential for MS analysis was chosen on the basis of the cyclic voltammetry (CV) study presented in the Figure 9a inset. The peaks observed at the CV curve are probably related to the V center oxidation/reduction with the simultaneous K^+ intercalation/deintercalation process. The impedance spectra were measured between 0.4 and 0.9 V vs Ag/AgCl (3 M KCl), but the linear behavior of $1/C_{sc}^2$ vs E was found between 0.58 and 0.69 V (see Figure 8a). The positive slope of the Mott−Schottky plot confirmed that the obtained nonhydrated KV_3O_8 phase is an n-type semiconductor and E_{fb} equals to about 0.56 V vs Ag/AgCl (3 M KCl) (0.765 V vs NHE). The energy band diagram was prepared assuming that E_{fb} lies just below the conduction band and the UV−vis determined indirect energy band gap of KV_3O_8 is 1.91 eV. As presented in Figure 8b, the valence band (VB) location allows photoexcited holes to react with adsorbed water and form hydroxyl radicals. On the other hand, the potential of the photoexcited electrons from the conduction band (CB) is not enough to form superoxide radicals. These conclusions are consistent with the efficiency of the photocatalysts.

According to the above-described results, the possible mechanism of photocatalytic performance of KV_3O_8 has been proposed. The major reaction steps responsible for the photocatalytic activity could be expressed as follows:

(1) $KV_3O_8 + h\nu \rightarrow e^-(CB, KV_3O_8) + h^+(CB, KV_3O_8)$

(2) $e^- + O_2 \rightarrow O_2^{\cdot -}$

(3) $h^+ + H_2O/OH^- \rightarrow OH\cdot$

(4) $OH\cdot + MB \rightarrow$ other product $\rightarrow CO_2 + H_2O$

(5) $h^+(CB, KV_3O_8) + MB$

$\rightarrow$ other product

$\rightarrow CO_2 + H_2O$

The UPLC−QTOF-MS/MS was further applied to identify the main MB degradation products for samples obtained after photocatalytic degradation by KVO-80 (KV_3O_8) and KVO-20 ($K_2V_6O_{16}\cdot 0.65H_2O$) used as a catalyst. The total ion current chromatograms (TICs, Supporting Information) are presented in Figure S6. On the basis of the received data after using KVO-80 as a catalyst, besides the nondecomposed MB, two additional degradation compounds were identified. The observed peaks on the chromatogram at 2.576 and 8.122 min correspond probably to 4-nitroaniline $[C_6H_6N_2O_2 + H]^+$ and m/z 139.0512, and phenol $[C_6H_6O + H]^+$ and m/z 95.0494, respectively (see Figure S7, Supporting Information), while the peak observed at 4.591 min is attributed to MB. The above photodegradation process generates about 8.34% of nondecomposed MB, 0.12% of aniline, and 0.45% of phenol. The possible degradation pathway where the aniline occurred as a product was described elsewhere.[82]

In the case of analysis of MB degradation products using KVO-20 as the photocatalyst, the obtained results allowed for the identification of at least four additional compounds besides MB residues (4.586 min, see Figure S8). The observed peaks on the chromatogram at 2.604 and 8.116 min in the resulting products, as in the case of KVO-80 catalyst, can be assigned to 4-nitroaniline $[C_6H_6N_2O_2 + H]^+$ and m/z 139.0508, and phenol $[C_6H_6O + H]^+$ and m/z 95.0494, respectively. Analysis of the sample after the use of KVO-20 as a catalyst also identifies two additional compounds. On the chromatogram at 3.12 min, the $[C_7H_{10}N_2O_4S + H]^+$ and m/z 219.0444 was identified, corresponding to 2-amino-5-(methylamino)-hydroxybenzenesulfonic acid, which was previously described in the photocatalytic MB degradation pathway,[83] which leads to H_2O and CO_2. In addition, it is worth mentioning that on the chromatogram peak presence at 5.219 min reveal to benzenesulfonic acid $[C_6H_6O_3S + H]^+$ and m/z 159.0063, which also occur in the photocatalytic MB degradation pathway as previously described.[84] Comparing the efficiency of MB degradation through the use of the KVO-20 catalyst with the KVO-80 catalyst, the efficiency of the KVO-20 catalyst is significantly lower. The photodegradation process catalyzed by KVO-20 generates about 16.78% of nondecomposed MB, 36.27% of benzenesulfonic acid, and comparable amounts (0.40%) of phenol and the amino-5-(methylamino)-hydroxybenzenesulfonic acid, which is formed in approximately 0.46%. On the other hand, a negligible 0.07% amount of 4-nitroaniline is formed when the KVO-20 catalyst was applied, which indicates the efficiency and difference of the photodegradation mechanisms of MB using the described catalysts.

CONCLUSIONS

In this study, $K_2V_6O_{16}\cdot 0.65H_2O$ nanobelts and KV_3O_8 microplatelets were synthesized using the facile LPE-IonEx method and investigated as catalysts for organic dye degradation. The obtained samples were characterized using XRD, FTIR, XPS,PPMS, UV−vis DRS, PL, TGA with MS, SEM, and N_2 adsorption isotherms. Controlling the reaction temperature (20−80 °C) resulted in various phase compositions, morphologies, and surface areas. Moreover, different synthesis temperatures provided varied concentrations of V^{4+} (from 9% up to such a high content as 62%). The photocatalytic degradation of methylene blue, under simulated solar light illumination, was examined to evaluate the photocatalytic performance of prepared samples. All samples acted as efficient photocatalysts, resulting in approximately 90% degradation of the dye within the first 30−90 min. The highest activity was observed for the sample obtained at 80 °C. According to the scavenger test, OH radicals and holes are the main active species in the case of $K_2V_6O_{16}\cdot 0.65H_2O$. The role of direct oxidation in the case of KV_3O_8 is smaller but still significant. The results indicate that potassium vanadates are potential candidates for light-driven photocatalysts. The observed excellent photocatalytic performances result from the specific structural properties, which were provided by the proposed innovative LPE-IonEx method. We suggest that it can be attributed to the high content of V^{4+} species in the samples, which traps electrons and facilitates charge separation.

https://doi.org/10.1021/acs.inorgchem.2c00136
Inorg. Chem. 2022, 61, 9433−9444

■ ASSOCIATED CONTENT

Supporting Information

The Supporting Information is available free of charge at https://pubs.acs.org/doi/10.1021/acs.inorgchem.2c00136.

TG and DTG curves with ion current curves of the KVO-20 sample; DSC curves of the KVO-20 and KVO-80 sample; FTIR, XRD, and SEM image of sample KVO-20 after heat treatment; XRD of as-prepared sample KVO-80 and XRD and XPS of KVO-80 deposited onto degreased FTO (KVO-80/FTO); results of MB photodegradation presented as the $\ln(C/C_0)$ vs time plots; and UPLC−QTOF-MS/MS (chromatograms and mass spectra) of MB degradation products for samples obtained after photocatalytic degradation by KVO-80 and KVO-20 (PDF)

■ AUTHOR INFORMATION

Corresponding Author

Marta Prześniak-Welenc − *Faculty of Applied Physics and Mathematics, Institute of Nanotechnology and Materials Engineering, Gdansk University of Technology, Gdansk 80-233, Poland;* orcid.org/0000-0002-7640-2677; Email: marwelen@pg.edu.pl

Authors

Małgorzata Nadolska − *Faculty of Applied Physics and Mathematics, Institute of Nanotechnology and Materials Engineering, Gdansk University of Technology, Gdansk 80-233, Poland;* orcid.org/0000-0001-5998-2975

Mariusz Szkoda − *Faculty of Chemistry, Gdansk University of Technology, Gdansk 80-233, Poland*

Konrad Trzciński − *Faculty of Chemistry, Gdansk University of Technology, Gdansk 80-233, Poland*

Paweł Niedziałkowski − *Faculty of Chemistry, University of Gdansk, Gdansk 80-308, Poland*

Jacek Ryl − *Faculty of Applied Physics and Mathematics, Institute of Nanotechnology and Materials Engineering, Gdansk University of Technology, Gdansk 80-233, Poland;* orcid.org/0000-0002-0247-3851

Aleksandra Mielewczyk-Gryń − *Faculty of Applied Physics and Mathematics, Institute of Nanotechnology and Materials Engineering, Gdansk University of Technology, Gdansk 80-233, Poland;* orcid.org/0000-0001-6795-3840

Karolina Górnicka − *Faculty of Applied Physics and Mathematics, Institute of Nanotechnology and Materials Engineering, Gdansk University of Technology, Gdansk 80-233, Poland*

Complete contact information is available at: https://pubs.acs.org/10.1021/acs.inorgchem.2c00136

Author Contributions

The manuscript was written through contributions of all authors. All authors have given approval to the final version of the manuscript.

Notes

The authors declare no competing financial interest.

■ ACKNOWLEDGMENTS

The authors would like to acknowledge Professor M. Sawczak from The Szewalski Institute of Fluid-Flow Machinery Polish Academy of Sciences for PL and UV−VIS enabling measurements. This work is supported by the National Science Center of Poland (Grant 2020/37/N/ST5/03697). The authors also acknowledge the financial support from Gdańsk University of Technology by the DEC-3/2020/IDUB/I.3.3 grant under the Argentum-"Excellence Initiative-Research University" and the National Centre for Research and Development via Grant LIDER/15/0088/L-10/18/NCBR/2019 (Integrated prototype of a photo-supercapacitor for energy storage obtained as a result of solar radiation conversion).

■ REFERENCES

(1) Melchionna, M.; Fornasiero, P. Updates on the Roadmap for Photocatalysis. *ACS Catal.* **2020**, *10*, 5493−5501.

(2) Anwer, H.; Mahmood, A.; Lee, J.; Kim, K. H.; Park, J. W.; Yip, A. C. K. Photocatalysts for Degradation of Dyes in Industrial Effluents: Opportunities and Challenges. *Nano Res.* **2019**, *12*, 955−972.

(3) Di Paola, A.; García-López, E.; Marcì, G.; Palmisano, L. A Survey of Photocatalytic Materials for Environmental Remediation. *J. Hazard. Mater.* **2012**, *211-212*, 3−29.

(4) Nazri, M. K. H. M.; Sapawe, N. A Short Review on Photocatalytic toward Dye Degradation. *Mater. Today: Proc.* **2020**, *31*, A42−A47.

(5) Nagajyothi, P. C.; Prabhakar Vattikuti, S. V.; Devarayapalli, K. C.; Yoo, K.; Shim, J.; Sreekanth, T. V. M. Green Synthesis: Photocatalytic Degradation of Textile Dyes Using Metal and Metal Oxide Nanoparticles-Latest Trends and Advancements. *Crit. Rev. Environ. Sci. Technol.* **2020**, *50*, 2617−2723.

(6) Marimuthu, S.; Antonisamy, A. J.; Malayandi, S.; Rajendran, K.; Tsai, P. C.; Pugazhendhi, A.; Ponnusamy, V. K. Silver Nanoparticles in Dye Effluent Treatment: A Review on Synthesis, Treatment Methods, Mechanisms, Photocatalytic Degradation, Toxic Effects and Mitigation of Toxicity. *J. Photochem. Photobiol. B Biol.* **2020**, *205*, No. 111823.

(7) Koe, W. S.; Lee, J. W.; Chong, W. C.; Pang, Y. L.; Sim, L. C. An Overview of Photocatalytic Degradation: Photocatalysts, Mechanisms, and Development of Photocatalytic Membrane. *Environ. Sci. Pollut. Res.* **2020**, *27*, 2522−2565.

(8) Chandrasekaran, S.; Yao, L.; Deng, L.; Bowen, C.; Zhang, Y.; Chen, S.; Lin, Z.; Peng, F.; Zhang, P. Recent Advances in Metal Sulfides: From Controlled Fabrication to Electrocatalytic, Photocatalytic and Photoelectrochemical Water Splitting and Beyond. *Chem. Soc. Rev.* **2019**, *48*, 4178−4280.

(9) Ayodhya, D.; Veerabhadram, G. A Review on Recent Advances in Photodegradation of Dyes Using Doped and Heterojunction Based Semiconductor Metal Sulfide Nanostructures for Environmental Protection. *Mater. Today Energy* **2018**, *9*, 83−113.

(10) Hasija, V.; Raizada, P.; Sudhaik, A.; Sharma, K.; Kumar, A.; Singh, P.; Jonnalagadda, S. B.; Thakur, V. K. Recent Advances in Noble Metal Free Doped Graphitic Carbon Nitride Based Nanohybrids for Photocatalysis of Organic Contaminants in Water: A Review. *Appl. Mater. Today* **2019**, *15*, 494−524.

(11) Dong, J. P.; Shi, Z. Z.; Li, B.; Wang, L. Y. Synthesis of a Novel 2D Zinc(Ii) Metal-Organic Framework for Photocatalytic Degradation of Organic Dyes in Water. *Dalt. Trans.* **2019**, *48*, 17626−17632.

(12) Wu, Y.; Luo, H.; Wang, H. Synthesis of Iron(Iii)-Based Metal-Organic Framework/Graphene Oxide Composites with Increased Photocatalytic Performance for Dye Degradation. *RSC Adv.* **2014**, *4*, 40435−40438.

(13) Hasanpour, M.; Hatami, M. Photocatalytic Performance of Aerogels for Organic Dyes Removal from Wastewaters: Review Study. *J. Mol. Liq.* **2020**, *309*, No. 113094.

(14) Ghiyasiyan-Arani, M.; Masjedi-Arani, M.; Salavati-Niasari, M. Facile Synthesis, Characterization and Optical Properties of Copper Vanadate Nanostructures for Enhanced Photocatalytic Activity. *J. Mater. Sci.: Mater. Electron.* **2016**, *27*, 4871−4878.

(15) Huang, Z. F.; Pan, L.; Zou, J. J.; Zhang, X.; Wang, L. Nanostructured Bismuth Vanadate-Based Materials for Solar-Energy-Driven Water Oxidation: A Review on Recent Progress. *Nanoscale* **2014**, *6*, 14044−14063.

(16) Xiang, L.; Fan, J.; Zhong, W.; Mao, L.; You, K.; Yin, D. Heteroatom-Induced Band-Reconstruction of Metal Vanadates for Photocatalytic Cyclohexane Oxidation towards KA-Oil Selectivity. *Appl. Catal., A* **2019**, *575*, 120−131.
(17) Guo, J.; Liang, J.; Yuan, X.; Jiang, L.; Zeng, G.; Yu, H.; Zhang, J. Efficient Visible-Light Driven Photocatalyst, Silver (Meta)Vanadate: Synthesis, Morphology and Modification. *Chem. Eng. J.* **2018**, *352*, 782−802.
(18) Zhao, X.; Huang, J.; Feng, L.; Cao, L.; Li, J.; Zhou, L. Facile Synthesis of α-Ag3VO4 Hollow Nanospheres with Improved Photocatalytic Activities. *J. Alloys Compd.* **2017**, *718*, 7−14.
(19) Wang, F.; Zhang, H.; Liu, L.; Shin, B.; Shan, F. AgV7O18: A New Silver Vanadate Semiconductor with Photodegradation Ability on Dyes under Visible-Light Irradiation. *Mater. Lett.* **2016**, *169*, 82−85.
(20) Khan, I.; Qurashi, A. Shape Controlled Synthesis of Copper Vanadate Platelet Nanostructures, Their Optical Band Edges, and Solar-Driven Water Splitting Properties. *Sci. Rep.* **2017**, *7*, 1−11.
(21) Sajid, M. M.; Zhai, H.; Shad, N. A.; Shafique, M.; Afzal, A. M.; Javed, Y.; Khan, S. B.; Ikram, M.; Amin, N.; Zhang, Z. Photocatalytic Performance of Ferric Vanadate (FeVO4) Nanoparticles Synthesized by Hydrothermal Method. *Mater. Sci. Semicond. Process.* **2021**, *129*, No. 105785.
(22) Li, D.; Bai, X.; Pan, C.; Zhu, Y. Investigations on the Phase Transition between CdV2O6 and Cd2V2O7 and Their Photocatalytic Performances. *Eur. J. Inorg. Chem.* **2013**, 3070−3075.
(23) Yang, R.; Zhang, Y.; Fan, Y.; Wang, R.; Zhu, R.; Tang, Y.; Yin, Z.; Zeng, Z. InVO4-Based Photocatalysts for Energy and Environmental Applications. *Chem. Eng. J.* **2022**, *428*, No. 131145.
(24) Mazierski, P.; Sowik, J.; Miodyńska, M.; Trykowski, G.; Mikołajczyk, A.; Klimczuk, T.; Lisowski, W.; Nadolna, J.; Zaleska-Medynska, A. Shape-Controllable Synthesis of GdVO 4 Photocatalysts and Their Tunable Properties in Photocatalytic Hydrogen Generation. *Dalt. Trans.* **2019**, *48*, 1662−1671.
(25) Wang, L.; Shi, X.; Jia, Y.; Cheng, H.; Wang, L.; Wang, Q. Recent Advances in Bismuth Vanadate-Based Photocatalysts for Photoelectrochemical Water Splitting. *Chin. Chem. Lett.* **2021**, *32*, 1869−1878.
(26) Sajid, M. M.; Amin, N.; Shad, N. A.; khan, S. B.; Javed, Y.; Zhang, Z. Hydrothermal Fabrication of Monoclinic Bismuth Vanadate (m-BiVO 4) Nanoparticles for Photocatalytic Degradation of Toxic Organic Dyes. *Mater. Sci. Eng., B* **2019**, *242*, 83−89.
(27) Monsef, R.; Ghiyasiyan-Arani, M.; Salavati-Niasari, M. Application of Ultrasound-Aided Method for the Synthesis of NdVO4 Nano-Photocatalyst and Investigation of Eliminate Dye in Contaminant Water. *Ultrason. Sonochem.* **2018**, *42*, 201−211.
(28) Sivakumar, V.; Suresh, R.; Giribabu, K.; Narayanan, V. BiVO 4 Nanoparticles: Preparation, Characterization and Photocatalytic Activity. *Cogent Chem.* **2015**, *1*, 1074647.
(29) Roy, J. S.; Dugas, G.; Morency, S.; Ribeiro, S. J. L.; Messaddeq, Y. Enhanced Photocatalytic Activity of Silver Vanadate Nanobelts in Concentrated Sunlight Delivered through Optical Fiber Bundle Coupled with Solar Concentrator. *SN Appl. Sci.* **2020**, *2*, 1−11.
(30) Pei, L. Z.; Lin, N.; Wei, T.; Yu, H. Y. Synthesis of Manganese Vanadate Nanobelts and Their Visible Light Photocatalytic Activity for Methylene Blue. *J. Exp. Nanosci.* **2016**, *11*, 197−214.
(31) Wang, W.; Yu, Y.; An, T.; Li, G.; Yip, H. Y.; Yu, J. C.; Wong, P. K. Visible-Light-Driven Photocatalytic Inactivation of E. Coli K-12 by Bismuth Vanadate Nanotubes: Bactericidal Performance and Mechanism. *Environ. Sci. Technol.* **2012**, *46*, 4599−4606.
(32) Kása, Z.; Almási, E. E.; Hernádi, K.; Gyulavári, T.; Baia, L.; Veréb, G.; László, Z.; Pap, Z. New Insights into the Photoactivity of Shape-Tailored BiVO4 Semiconductors via Photocatalytic Degradation Reactions and Classical Reduction Processes. *Molecules* **2020**, *25*, 1−14.
(33) Chen, L.; Wang, J.; Meng, D.; Wu, X.; Wang, Y.; Zhong, E. The PH-Controlled {040} Facets Orientation of BiVO4 Photocatalysts with Different Morphologies for Enhanced Visible Light Photocatalytic Performance. *Mater. Lett.* **2016**, *162*, 150−153.
(34) Zhang, K.; Deng, J.; Liu, Y.; Xie, S.; Dai, H. Photocatalytic Removal of Organics over BiVO4-Based Photocatalysts. In *Materials, Mechanisms and Applications, Wenbin Cao, IntechOpen*.
(35) Wu, M.; Jing, Q.; Feng, X.; Chen, L. BiVO 4 Microstructures with Various Morphologies: Synthesis and Characterization. *Appl. Surf. Sci.* **2018**, *427*, 525−532.
(36) Zhao, Y.; Li, R.; Mu, L.; Li, C. Significance of Crystal Morphology Controlling in Semiconductor-Based Photocatalysis: A Case Study on BiVO4 Photocatalyst. *Cryst. Growth Des.* **2017**, *17*, 2923−2928.
(37) Tokunaga, S.; Kato, H.; Kudo, A. Selective Preparation of Monoclinic and Tetragonal BiVO4 with Scheelite Structure and Their Photocatalytic Properties. *Chem. Mater.* **2001**, *13*, 4624−4628.
(38) Li, W.; Wang, X.; Wang, Z.; Meng, Y.; Sun, X.; Yan, T.; You, J.; Kong, D. Relationship between Crystalline Phases and Photocatalytic Activities of BiVO4. *Mater. Res. Bull.* **2016**, *83*, 259−267.
(39) Thalluri, S. M.; Hussain, M.; Saracco, G.; Barber, J.; Russo, N. Green-Synthesized BiVO4 Oriented along {040} Facets for Visible-Light-Driven Ethylene Degradation. *Ind. Eng. Chem. Res.* **2014**, *53*, 2640−2646.
(40) Kamble, G. S.; Ling, Y. C. Solvothermal Synthesis of Facet-Dependent BiVO4 Photocatalyst with Enhanced Visible-Light-Driven Photocatalytic Degradation of Organic Pollutant: Assessment of Toxicity by Zebrafish Embryo. *Sci. Rep.* **2020**, *10*, 1−11.
(41) Bakhtiarnia, S.; Sheibani, S.; Billard, A.; Sun, H.; Aubry, E.; Yazdi, M. A. P. Enhanced Photocatalytic Activity of Sputter-Deposited Nanoporous BiVO4 Thin Films by Controlling Film Thickness. *J. Alloys Compd.* **2021**, *879*, No. 160463.
(42) Pham, M. Q.; Ngo, T. M.; Nguyen, V. H.; Nong, L. X.; Vo, D. V. N.; Van Tran, T.; Nguyen, T. D.; Bui, X. T.; Nguyen, T. D. Facile Solvothermal Synthesis of Highly Active Monoclinic Scheelite BiVO4 for Photocatalytic Degradation of Methylene Blue under White LED Light Irradiation. *Arab. J. Chem.* **2020**, *13*, 8388−8394.
(43) Pantò, F.; Dahrouch, Z.; Saha, A.; Patanè, S.; Santangelo, S.; Triolo, C. Photocatalytic Degradation of Methylene Blue Dye by Porous Zinc Oxide Nanofibers Prepared via Electrospinning: When Defects Become Merits. *Appl. Surf. Sci.* **2021**, *557*, No. 149830.
(44) Shi, C.; Dong, X.; Wang, J.; Wang, X.; Ma, H.; Zhang, X. Interfacial Defect Engineering over Fusiform Bismuth Vanadate Photocatalyst Enables to Excellent Solar-to-Chemical Energy Coupling. *RSC Adv.* **2017**, *7*, 26717−26721.
(45) Wen, P.; Liu, T.; Wei, F.; Ai, L.; Yao, F. Soft Chemical Topotactic Synthesis and Crystal Structure Evolution from Two-Dimensional KV3O8 Plates to One-Dimensional V3O7 Nanobelts. *CrystEngComm* **2016**, *18*, 8880−8886.
(46) Miller, D. J.; Biesinger, M. C.; McIntyre, N. S. Interactions of CO2 and CO at Fractional Atmosphere Pressures with Iron and Iron Oxide Surfaces: One Possible Mechanism for Surface Contamination? *Surf. Interface Anal.* **2002**, *33*, 299−305.
(47) López, R.; Gómez, R. Band-Gap Energy Estimation from Diffuse Reflectance Measurements on Sol−Gel and Commercial TiO2: A Comparative Study. *J. Sol-Gel Sci. Technol.* **2012**, *61*, 1−7.
(48) Trzciński, K.; Szkoda, M.; Herman, A.; Borowska-Centkowska, A.; Lisowska-Oleksiak, A. Does the Low Optical Band Gap of Yellow Bi3YO6 Guarantee the Photocatalytical Activity under Visible Light Illumination? *J. Solid State Electrochem.* **2018**, *22*, 2095−2105.
(49) Bai, L.; Xue, Y.; Zhang, J.; Pan, B.; Wu, C. Synthetic Potassium Vanadium Oxide K2V6O 16·1.5H2O Superlong Nanobelts: A 1D Room-Temperature Ferromagnetic Semiconductor. *Eur. J. Inorg. Chem.* **2013**, *20*, 3497−3505.
(50) Wang, C.; Cao, Y.; Luo, Z.; Li, G.; Xu, W.; Xiong, C.; He, G.; Wang, Y.; Li, S.; Liu, H.; Fang, D. Flexible Potassium Vanadate Nanowires on Ti Fabric as a Binder-Free Cathode for High-Performance Advanced Lithium-Ion Battery. *Chem. Eng. J.* **2017**, *307*, 382−388.
(51) Zavalij, P. Y.; Whittingham, M. S. Structural Chemistry of Vanadium Oxides with Open Frameworks. *Acta Crystallogr. Sect. B Struct. Sci.* **1999**, *55*, 627−663.

https://doi.org/10.1021/acs.inorgchem.2c00136
Inorg. Chem. 2022, 61, 9433−9444

(52) Frederickson, L. D.; Hausen, D. M. Infrared Spectra-Structure Correlation Study of Vanadium-Oxygen Compounds. *Anal. Chem.* **1963**, *35*, 818−827.
(53) Baddour-Hadjean, R.; Boudaoud, A.; Bach, S.; Emery, N.; Pereira-Ramos, J. P. A Comparative Insight of Potassium Vanadates as Positive Electrode Materials for Li Batteries: Influence of the Long-Range and Local Structure. *Inorg. Chem.* **2014**, *53*, 1764−1772.
(54) Wang, J.; Gao, G.; Zhou, X.; Wu, J.; Yang, H.; Li, Q.; Wu, G. A Facile Method to Prepare Bi-Phase Lithium Vanadate as Cathode Materials for Li-Ion Batteries. *J. Solid State Electrochem.* **2014**, *18*, 2459−2467.
(55) Li, L.; Liu, S.; Liu, W.; Ba, D.; Liu, W.; Gui, Q.; Chen, Y.; Hu, Z.; Li, Y.; Liu, J. Electrolyte Concentration Regulation Boosting Zinc Storage Stability of High-Capacity K0.486V2O5 Cathode for Bendable Quasi-Solid-State Zinc Ion Batteries. *Nano-Micro Lett.* **2021**, *13*, 1−14.
(56) Nakamoto, K. *Infrared and Raman Spectra of Inorganic and Coordination Compounds*; John Wiley & Sons, Ltd., 2008, DOI: 10.1002/9780470405888.fmatter.
(57) Linstrom, P. J.; Mallard, W. G. Mass Spectra. *In NIST Chemistry WebBook*; National Institute of Standards and Technology: Gaithersburg.
(58) Xie, Z.; Lai, J.; Zhu, X.; Wang, Y. Green Synthesis of Vanadate Nanobelts at Room Temperature for Superior Aqueous Rechargeable Zinc-Ion Batteries. *ACS Appl. Energy Mater.* **2018**, *1*, 6401−6408.
(59) Prześniak-Welenc, M.; Szreder, N. A.; Winiarski, A.; Łapiński, M.; Kościelska, B.; Barczyński, R. J.; Gazda, M.; Sadowski, W. Electrical Conductivity and Relaxation Processes in V2O5 Nanorods Prepared by Sol-Gel Method. *Phys. Status Solidi Basic Res.* **2015**, *252*, 2111.
(60) Silversmit, G.; Depla, D.; Poelman, H.; Marin, G. B.; De Gryse, R. Determination of the V2p XPS Binding Energies for Different Vanadium Oxidation States (V5+ to V0+). *J. Electron Spectros. Relat. Phenomena* **2004**, *135*, 167−175.
(61) Ambade, R. B.; Ambade, S. B.; Mane, R. S.; Lee, S. H. Interfacial Engineering Importance of Bilayered ZnO Cathode Buffer on the Photovoltaic Performance of Inverted Organic Solar Cells. *ACS Appl. Mater. Interfaces* **2015**, *7*, 7951−7960.
(62) Zakharova, G. S.; Täschner, C.; Kolb, T.; Jähne, C.; Leonhardt, A.; Büchner, B.; Klingeler, R. Morphology Controlled NH4V3O8 Microcrystals by Hydrothermal Synthesis. *Dalt. Trans.* **2013**, *42*, 4897−4902.
(63) Prześniak-Welenc, M.; Nadolska, M.; Kościelska, B.; Sadowska, K. Tailoring the Size and Shape — New Path for Ammonium Metavanadate Synthesis. *Materials* **2019**, *12*, 3446.
(64) Li, H.; Chen, Y.; Zhou, W.; Gao, H.; Tian, G. Tuning in BiVO 4 /Bi 4 V 2 O 10 Porous Heterophase Nanospheres for Synergistic Photocatalytic Degradation of Organic Pollutants. *Appl. Surf. Sci.* **2019**, *470*, 631−638.
(65) Kong, X.; Guo, Z.; Wen, P.; Huang, J.; Cao, L.; Yin, L.; Li, J.; Feng, Q. Controllable Synthesis and Morphology Evolution from Two-Dimensions to One-Dimension of Layered K2V6O16·nH2O. *CrystEngComm* **2015**, *17*, 3777−3782.
(66) Phanichphant, S.; Nakaruk, A.; Chansaenpak, K.; Channei, D. Evaluating the Photocatalytic Efficiency of the BiVO4/RGO Photocatalyst. *Sci. Rep.* **2019**, *9*, 1−9.
(67) Wang, Z.; Wang, J.; Pan, Y.; Liu, F.; Lai, Y.; Li, J.; Jiang, L. Preparation and Characterization of a Novel and Recyclable InVO4/ZnFe2O4 Composite for Methylene Blue Removal by Adsorption and Visible-Light Photocatalytic Degradation. *Appl. Surf. Sci.* **2020**, *501*, No. 144006.
(68) Wang, X.; Zhou, J.; Zhao, S.; Chen, X.; Yu, Y. Synergistic Effect of Adsorption and Visible-Light Photocatalysis for Organic Pollutant Removal over BiVO 4 /Carbon Sphere Nanocomposites. *Appl. Surf. Sci.* **2018**, *453*, 394−404.
(69) Wu, J. M.; Chen, Y.; Pan, L.; Wang, P.; Cui, Y.; Kong, D. C.; Wang, L.; Zhang, X.; Zou, J. J. Multi-Layer Monoclinic BiVO4 with Oxygen Vacancies and V4+ Species for Highly Efficient Visible-Light Photoelectrochemical Applications. *Appl. Catal. B Environ.* **2018**, *221*, 187−195.
(70) Cheng, C.; Fang, Q.; Fernandez-Alberti, S.; Long, R. Controlling Charge Carrier Trapping and Recombination in BiVO4-with the Oxygen Vacancy Oxidation State. *J. Phys. Chem. Lett.* **2021**, *12*, 3514−3521.
(71) Zhang, Y.; Guo, Y.; Duan, H.; Li, H.; Sun, C.; Liu, H. Facile Synthesis of V4+ Self-Doped, [010] Oriented BiVO4 Nanorods with Highly Efficient Visible Light-Induced Photocatalytic Activity. *Phys. Chem. Chem. Phys.* **2014**, *16*, 24519−24526.
(72) Guo, L.; Li, J.; Lei, N.; Song, Q.; Liang, Z. Morphological Evolution and Enhanced Photoelectrochemical Performance of V4+ Self-Doped, [010] Oriented BiVO4 for Water Splitting. *J. Alloys Compd.* **2019**, *771*, 914−923.
(73) Yu, R.; Xue, N.; Huo, S.; Li, J.; Wang, J. Structure Characteristics and Photoactivity of Simultaneous Luminescence and Photocatalysis in CaV2O6 Nanorods Synthesized by the Sol-Gel Pechini Method. *RSC Adv.* **2015**, *5*, 63502−63512.
(74) Saputera, W. H.; Amri, A. F.; Mukti, R. R.; Suendo, V.; Devianto, H.; Sasongko, D. Photocatalytic Degradation of Palm Oil Mill Effluent (Pome) Waste Using Bivo4 Based Catalysts. *Molecules* **2021**, *26*, 6225.
(75) Kumar, K. V.; Porkodi, K.; Rocha, F. Langmuir-Hinshelwood Kinetics - A Theoretical Study. *Catal. Commun.* **2008**, *9*, 82−84.
(76) Yang, M. Q.; Han, C.; Zhang, N.; Xu, Y. J. Precursor Chemistry Matters in Boosting Photoredox Activity of Graphene/Semiconductor Composites. *Nanoscale* **2015**, *7*, 18062−18070.
(77) Wu, J.; Lü, X.; Zhang, L.; Xia, Y.; Huang, F.; Xu, F. Crystallinity Control on Photocatalysis and Photoluminescence of TiO2-Based Nanoparticles. *J. Alloys Compd.* **2010**, *496*, 234−240.
(78) Liqiang, J.; Yichun, Q.; Baiqi, W.; Shudan, L.; Baojiang, J.; Libin, Y.; Wei, F.; Honggang, F.; Jiazhong, S. Review of Photoluminescence Performance of Nano-Sized Semiconductor Materials and Its Relationships with Photocatalytic Activity. *Sol. Energy Mater. Sol. Cells* **2006**, *90*, 1773−1787.
(79) Wu, P.; Li, Q.; Zou, X.; Cheng, W.; Zhang, D.; Zhao, C.; Chi, L.; Xiao, T. Correlation between Photoluminescence and Oxygen Vacancies in In 2O3, SnO2 and ZnO Metal Oxide Nanostructures. *J. Phys. Conf. Ser.* **2009**, 188.
(80) Kang, M.; Chu, M.; Kim, S. W.; Ryu, J. W. Optical and Electrical Properties of V2O5 Nanorod Films Grown Using an Electron Beam. *Thin Solid Films* **2013**, *547*, 198−201.
(81) Le, T. K.; Kang, M.; Kim, S. W. Morphology Engineering, Room-Temperature Photoluminescence Behavior, and Sunlight Photocatalytic Activity of V2O5 Nanostructures. *Mater. Charact.* **2019**, *153*, 52−59.
(82) Jia, P.; Tan, H.; Liu, K.; Gao, W. Synthesis, Characterization and Photocatalytic Property of Novel ZnO/Bone Char Composite. *Mater. Res. Bull.* **2018**, *102*, 45−50.
(83) Xia, S.; Zhang, L.; Pan, G.; Qian, P.; Ni, Z. Photocatalytic Degradation of Methylene Blue with a Nanocomposite System: Synthesis, Photocatalysis and Degradation Pathways. *Phys. Chem. Chem. Phys.* **2015**, *17*, 5345−5351.
(84) Houas, A.; Lachheb, H.; Ksibi, M.; Elaloui, E.; Guillard, C.; Herrmann, J. M. Photocatalytic Degradation Pathway of Methylene Blue in Water. *Appl. Catal. B Environ.* **2001**, *31*, 145−157.

https://doi.org/10.1021/acs.inorgchem.2c00136
Inorg. Chem. 2022, 61, 9433−9444